

Nanoscale inclusions in the phonon glass thermoelectric material Zn_4Sb_3

Ø. Prytz^{a*}, A.E. Gunnæs^a, O.B. Karlsen^a, T.H. Breivik^a, E.S. Toberer^b,
G. Jeffrey Snyder^b and J. Taftø^a

^aDepartment of Physics, University of Oslo, P.O. Box 1048 Blindern, NO-0316 Oslo, Norway; ^bDepartment of Materials Science, California Institute of Technology, 1200 East California Boulevard, Pasadena, CA 91125, USA

(Received 13 January 2009; final version received 5 April 2009)

We have investigated the thermoelectric material Zn_4Sb_3 using transmission electron microscopy (TEM). Nanoscale inclusions with a diameter of about 10 nm were observed, constituting on the order of 1% by volume of the material. Studies using energy filtered imaging, electron diffraction, and high-angle annular dark-field STEM indicate that the inclusions consist of Zn. These inclusions are expected to scatter the medium and long-wavelength phonons effectively, thus contributing to phonon glass behavior which results in the exceptionally low thermal conductivity for this thermoelectric material.

Keywords: thermoelectric material; phonon glass; nanoparticles; TEM

1. Introduction

The thermoelectric material Zn_4Sb_3 has attracted much attention over the past decade due to its outstanding thermoelectric properties [1]. The quality of a thermoelectric material is measured by the so-called figure of merit $Z = \alpha^2 \sigma / (\kappa_e + \kappa_l)$, where α is the Seebeck coefficient, σ the electric conductivity, and κ_e and κ_l are the electronic and lattice contributions to the thermal conductivity. Thus, high values of the Seebeck coefficient and electric conductivity are wanted, while the total thermal conductivity should be low. However, since the electronic contribution to the thermal conductivity increases with increasing electric conductivity, a low lattice thermal conductivity is of paramount importance. This leads to the much used rule of thumb that a good thermoelectric material should be an ‘electron-crystal phonon-glass’ [2]: it should conduct electrons as a crystal, but scatter phonons as a glass.

While Zn_4Sb_3 has reasonable values of α and σ , it is the unusually low κ_l which is credited for the high figure of merit of Zn_4Sb_3 [1,2]. Indeed, this material is often cited as the prototypic ‘electron-crystal phonon-glass’, with low lattice thermal conductivity attributed to structural features which scatter phonons. While the basic structural framework of Zn_4Sb_3 (or more precisely $\text{Zn}_{3.9-\delta}\text{Sb}_3$) has been known for several decades [3], the discovery of partial Zn occupancy on several interstitial sites

*Corresponding author. Email: oystein.prytz@fys.uio.no

within the unit cell [4] has lead to a reexamination of the structure. Theoretical studies confirm the need for interstitial Zn atoms and indicate that the surrounding framework undergoes significant distortions to accommodate these interstitials [5]. Pair distribution function (PDF) analysis further confirms that the framework distorts around the interstitials and additionally suggests these interstitials exhibit short-range order despite the lack of long-range order in Zn_4Sb_3 [6].

We have investigated samples of nominal composition Zn_4Sb_3 using transmission electron microscopy (TEM) by combining bright-and dark-field imaging, electron diffraction, high-angle annular dark-field scanning TEM (HAADF-STEM), and energy filtered TEM (EFTEM). The main finding of these studies is that the material is richly nanostructured, containing nanoparticles on the 10 nm scale. Such features are expected to scatter medium and long-wavelength phonons, thereby contributing to the low lattice thermal conductivity of the system.

2. Experimental

The samples were prepared through reaction of the pure elements in sealed silica ampoules under vacuum. The mixtures were melted at 700°C for one day and lightly shaken to ensure a homogeneous melt. The melt was quenched in water and then annealed for one day at 300°C in the same ampoule before being water quenched again. Powder X-ray diffraction patterns could be indexed to the unit cell reported earlier for Zn_4Sb_3 at room temperature [3,4]. In addition, the diffraction data indicated the presence of small amounts of pure Zn. Using optical and scanning electron microscopy, Zn particles of several micrometers in diameter were detected. Samples for TEM were prepared by mechanical grinding and standard ion-milling techniques. Also, samples were prepared by crushing in ethanol and deposited on a carbon film suspended on a copper grid.

The electron diffraction and bright- and dark-field experiments were performed in a JEOL 2000FX TEM, while a JEOL 2010F microscope fitted with a Gatan imaging filter (GIF200) was used for the annular dark-field and energy filtered imaging.

3. Results and discussion

Selected area diffraction patterns could be indexed according to the structure reported earlier for Zn_4Sb_3 . While crystalline ring patterns attributed to a surface layer of ZnO were sometimes observed, no extra or split reflections were readily visible. Thus, no immediate evidence for secondary phases, twinning, or other crystal defects was observed in the typical crystal grains.

However, imaging using the directly transmitted electrons revealed that the samples are richly nanostructured, displaying particles on the nanometer scale as seen in Figure 1a. In thin areas, the particles display a very bright contrast regardless of crystal orientation, suggesting that they are composed of weak electron scatterers compared to the matrix. Meanwhile, high-resolution imaging confirmed the presence of nanosized inclusions within the crystal grains (Figure 2a). We performed an analysis of particle size, showing that the median particle size was 8.34 nm (Figure 1c). Estimates of the density of particles are difficult since the sample

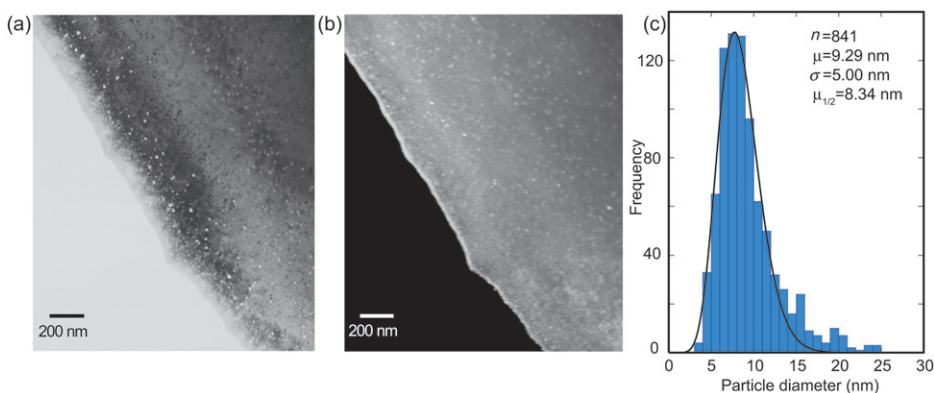


Figure 1. (a) Bright-field image from an area showing large amounts of nanoinclusions in the parent Zn_4Sb_3 phase. (b) Dark-field image formed by diffusely scattered electrons. (c) Histogram of the particle size distribution. The solid line is a fitted gamma function, while the average (μ) and median ($\mu_{1/2}$) particle size are given together with the standard deviation (σ) and number of measured particles (n).

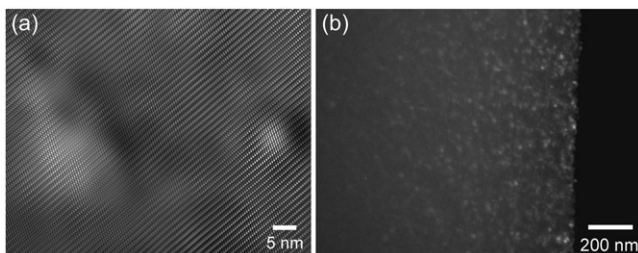


Figure 2. (a) Fourier-filtered high-resolution micrograph of nanoinclusions such as those seen in Figure 1. The observed lattice fringes are from the matrix, while the particles are visible as bright areas of lower effective thickness. (b) Dark-field image similar to that of Figure 1b, but from the cleaved edge of a crushed specimen.

thickness is not accurately known. However, in areas of 100 nm, estimated thickness of the particles make up in the order of 1 vol% of the material.

Figure 1b shows a dark-field image formed using electrons in the background of the diffraction pattern, between the Bragg reflections of the matrix. The nanoscale inclusions are clearly visible as small areas of bright contrast in this image. This may be attributed either to the image being formed by weak reflections from the inclusions, or by electrons scattered from defects or displacements in conjunction with the particles. Similar observations are made from the cleaved edges of crushed samples, providing strong evidence that the particles are not surface effects or artefacts due to the sample preparation (Figure 2b).

When the sample was tilted into the [001] projection (hexagonal setting) of Zn_4Sb_3 , heavily exposed diffraction patterns revealed weak extra reflections (Figure 3a). These reflections come in sets of three: one central reflection oriented parallel with the 600-type reflections of the parent phase, with two weaker satellites on either side. The d -value associated with these extra reflections corresponds to a plane spacing of $d=2.094 \pm 0.009 \text{ \AA}$. These diffraction patterns indicate the

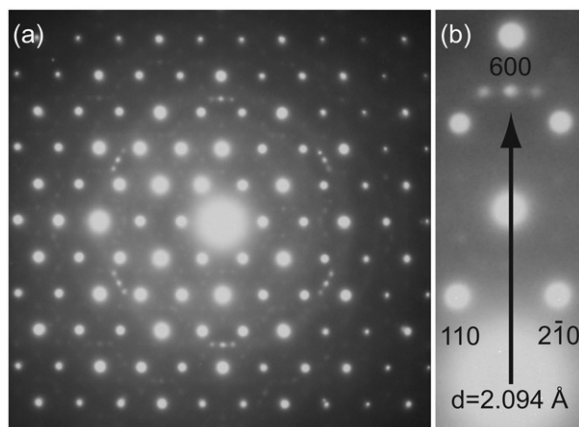


Figure 3. Selected area diffraction pattern taken with a long exposure time in the $[001]$ projection of the Zn_4Sb_3 phase. (b) Sets of extra reflections are observed close to the 600 and $6\bar{6}0$ -type reflections of the parent phase, and correspond to a d -value of $2.094 \pm 0.009 \text{ \AA}$.

presence of a secondary phase with well-defined orientation relationships to the parent phase. Nanoparticles of this size are commonly coherent because of reduced interfacial energy. There appears to be at least two symmetry relationships between the particles and the matrix: one associated with the central reflections and the other associated with the satellites. Coherent nanoparticles have also been observed in the thermoelectric $\text{AgSbTe}_2\text{-PbTe}$ materials [7].

Several phases should be considered as possible candidates to explain the observed particles. Pure metals Sb and Zn, as well as ZnSb are stable at room temperature, and oxides such as ZnO are possible. Of these, only hexagonal Zn has a strong reflection ($d_{101}=2.091 \text{ \AA}$) close to our observations. While the Zn-rich Zn_3Sb_2 has a strong reflection at $d=2.088 \text{ \AA}$ [8], this phase is not stable below approximately 400°C [9].

In order to clarify the nature of the observed particles, we performed imaging, and HAADF-STEM. In EFTEM imaging, only electrons that have suffered a particular energy loss when passing through the specimen are used to form the image. As different elements and phases may cause different energy losses for the electron beam, this enables us to create images that map the spatial distribution of a phase or an element [10]. Figure 4a shows the energy loss spectrum obtained from a large area of Zn_4Sb_3 together with that of metallic zinc [11]. Both materials have an intensity maximum at an energy loss of 15 eV, corresponding to collective excitations of the valence electrons (plasmon excitations). However, metallic Zn displays a significant shoulder at approximately 10 eV. Figure 4b shows energy filtered images formed with electrons from the three energy loss regions (A–C) indicated in Figure 4a. The nanoscale particles are clearly visible when using the elastically scattered electrons to form the image (energy region A), but virtually all matrix–particle contrast is gone when using the electrons that have lost energy to plasmon excitations (energy region C). For the intermediate energy range (energy region B) the particles are brighter than the surrounding matrix, thus indicating that they contain significantly higher concentration of Zn than the matrix.

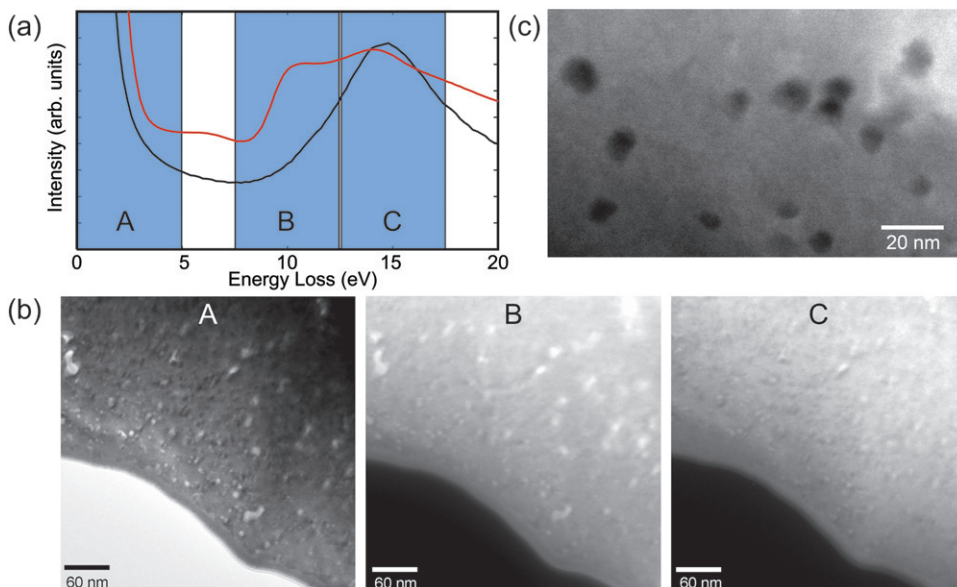


Figure 4. (Color online). (a) Energy loss spectra of Zn_4Sb_3 (black) and pure Zn (red). Pure Zn displays a significant shoulder at 10 eV energy loss, thus allowing us to differentiate between the matrix and Zn particles using EFTEM imaging. The three energy loss regions used are indicated (A–C). (b) EFTEM images from a region containing nanoparticles. The images were formed with a 10 eV slit centered on the zero loss peak (A), and a 5 eV slit centered on 10 and 15 eV (B and C) as indicated in (a). (c) HAADF-STEM Z-contrast image showing the particles as dark areas, indicating a low average atomic number than the matrix.

Further evidence that the particles are Zn comes from observations that indicate the particles are composed of weaker electron scatterers (lower atomic number) than the matrix. Bright-field images, including orientations where strong reflections from the parent phase are absent, suggest that the particles have a high electron transmittivity compared to the matrix. In experiments using HAADF-STEM, the particles appear as dark areas (Figure 4c). In these experiments, only electrons scattered to large angles are used to form the image. Heavy elements scatter electrons to larger angles and give a higher intensity in the image than light elements. The technique is sensitive to differences in atomic number, giving intensity variations roughly proportional to the atomic number squared [12,13]. These observations indicate that the particles have a significantly lower average atomic number than the surrounding matrix; thus, nanoparticles of pure Zn can explain all the observations.

These observations may resolve contradictions in the literature on the Zn_4Sb_3 system, and may furthermore provide an explanation of the very low lattice thermal conductivity. X-ray diffraction results [4,14,15] consistently indicate significantly less Zn than the nominal 4:3 ratio of Zn_4Sb_3 . For example, a composition of $Zn_{3.83}Sb_3$ was determined in a previous work [4]. However, according to phase diagram determinations [9] Zn_4Sb_3 forms in a narrow composition range between $Zn_{3.90}Sb_3$ and $Zn_{3.98}Sb_3$. Small nanoparticles of Zn embedded in the matrix would be included

in the typical chemical analysis (e.g. microprobe or EDX) of apparently single phase grains used for phase identification or phase diagram determination, but would not contribute to the diffraction of Zn_4Sb_3 . We estimate that the particles make up in the order of 1% by volume of the material. This is equivalent to $\delta \approx 0.1$, and can partially account for the differences in observed Zn content.

The bimodal size-distribution of Zn inclusions (on both the 10 nm and 1 μm scale) indicates two Zn formation steps. While the high-temperature phase diagram is complex and under some dispute, the existence of large Zn grains indicates that the specimen was at one time in a two phase region between Zn_4Sb_3 and Zn at high enough temperature for the Zn to coalesce into micrometer-sized particles. However, the presence of nanometer-sized Zn particles indicates there must have been an additional formation step at low temperature where diffusion is slow.

Small nanometer-sized Zn particles can be explained via a low-temperature precipitation mechanism. Generally, precipitation occurs when solubility (of Zn in $\text{Zn}_{3.9-\delta}\text{Sb}_3$ in this case) decreases with temperature due to the effect of entropy. From the presence of the micron-sized Zn grains, we know the composition of $\text{Zn}_{3.9-\delta}\text{Sb}_3$ must have been at the Zn-rich Zn_4Sb_3 phase boundary when formed at high temperatures (possibly the melt). As the maximum Zn content in $\text{Zn}_{3.9-\delta}\text{Sb}_3$ decreases as the sample further cools, precipitation of small particles of Zn results. The coarsening of the small Zn particles is suppressed at these lower temperatures. By this mechanism, the formation and even existence of these particles is dependent on composition and cooling procedure.

An understanding of the lattice thermal conductivity in Zn_4Sb_3 is thereby complicated by several phonon scattering sources which may be working in conjunction. Indeed, in recent years there has been an increasing focus on the role of nanostructures in reducing the lattice thermal conductivity of materials through phonon scattering [16]. The presence of either naturally occurring or artificially grown nanoparticles has been shown to strongly influence the thermal conductivity in several materials. Zhang and co-workers observed a reduction in the thermal conductivity of Mg–Si–Sn alloys attributed to naturally occurring nanostructures on the 10 nm scale [17], while a 50% reduction in the thermal conductivity of $\text{In}_{0.53}\text{Ga}_{0.47}\text{As}$ was achieved by Kim et al. [18] when embedding ErAs particles. The low thermal conductivity in the AgSbTe_2 –PbTe materials has also been attributed to similar sized nanoparticles [7]. Nanoparticles with the size and distribution we observe in Zn_4Sb_3 can thus be expected to effectively scatter medium and long-wavelength phonons [18]. At the same time, the disordered local structure within the crystal unit cell of Zn_4Sb_3 [4] contributes to the scattering of shorter wavelength phonons, with k-vectors around the Brillouin zone boundary. Thus, these features, on both the sub-nanometer and 10 nm scale, may contribute to the exceptionally low κ_l of Zn_4Sb_3 .

However, processing has been shown to dramatically effect both the electronic and thermal transport properties [1,19,20]. The occurrence of Zn nanoparticles, which likely depends on processing parameters, may explain some of these differences. If the high-temperature solubility explanation is correct, these nanoparticles may re-incorporate into the Zn_4Sb_3 during high temperature measurements, which would lead to varying transport properties and hysteresis. Also, the distribution of these inclusions on a large scale is difficult to assess using TEM.

Techniques such as small angle X-ray or neutron scattering may be appropriate to determine the prevalence of the particles on a more global scale [21].

4. Conclusions

Our TEM observations reveal Zn nanoparticles embedded in grains of $\text{Zn}_{3.9-8}\text{Sb}_3$. These inclusions likely precipitate from Zn-rich Zn_4Sb_3 due to a decreasing solubility of Zn upon cooling. This phase behavior reconciles previous crystallographic investigations with phase diagram determinations that indicate a higher Zn content. We expect that the presence of nanoparticles contributes to phonon glass behavior and the low thermal conductivity of Zn_4Sb_3 , and that processing conditions and starting stoichiometry likely explain the variance in thermoelectric properties found in the literature.

Acknowledgements

The authors would like to acknowledge financial support from the Norwegian Research Council and the Caltech MURI program. We would also like to thank Douglas Medlin for discussions.

References

- [1] T. Caillat, J.P. Fleurial and A. Borshchevsky, *J. Phys. Chem. Solid.* 58 (1997) p.1119.
- [2] G.J. Snyder and E.S. Toberer, *Nat. Mater.* 7 (2008) p.105.
- [3] H.W. Mayer, I. Mikhail and K. Schubert, *J. Less-Common Metals* 59 (1978) p.43.
- [4] G.J. Snyder, M. Christensen, W. Nishibori, T. Caillat and B.B. Iversen, *Nat. Mater.* 3 (2004) p.458.
- [5] E.S. Toberer, K.A. Sasaki, C.R.I. Chisholm, S.M. Haile, W.A. Goddard III and G.J. Snyder, *Phys. Status Solidi (RRL)* 1 (2007) p.253.
- [6] H.J. Kim, E.S. Bozin, S.M. Haile, G.J. Snyder and S.J.L. Billinge, *Phys. Rev. B* 75 (2007) p.134103.
- [7] K.F. Hsu, S. Loo, F. Guo, W. Chen, J.S. Dyck, C. Uher, T. Hogan, E.K. Polychroniadis and M.G. Kanatzidis, *Science* 303 (2004) p.818.
- [8] V.I. Psarev and K.A. Dobryden, *Inorg. Mater. USSR* 6 (1970) p.203.
- [9] V. Izard, M.C. Record, J.C. Tedenac and S.G. Fries, *Calphad* 25 (2001) p.567.
- [10] F. Hofer and P. Warbichler, *Elemental mapping using energy filtered imaging*, in *Transmission Electron Energy Loss Spectrometry in Materials Science and the EELS Atlas*, C.C. Ahn, ed., Wiley-VCH Verlag GmbH & Co. KGaA, Weinheim, Germany, 2004, Chap. 6, p.159.
- [11] C.C. Ahn (ed.), *Transmission Electron Energy Loss Spectrometry in Materials Science and the EELS Atlas*, Vol. 2, Wiley-VCH Verlag GmbH & Co. KGaA, Weinheim, 2004.
- [12] S.J. Pennycook and L.A. Boatner, *Nature* 336 (1988) p.565.
- [13] I. Arslan, T.J.V. Yates, N.D. Browning and P.A. Midgley, *Science* 309 (2005) p.2195.
- [14] G.J. Snyder, P.W. Stephens and S.M. Haile, *Synchrotron X-ray structure refinement of Zn_4Sb_3 in Proceedings ICT '05, Clemson*, International Thermoelectric Society, IEEE, 2005, p.312.
- [15] F. Cargnoli, E. Nishibori, P. Rabiller, Luca Bertini, G.J. Snyder, M. Christensen, C. Gatti and B.B. Iversen, *Chem. A Euro. J.* 10 (2004) p.3861.

- [16] M.S. Dresselhaus, G. Chen, M.Y. Tang, R. yang, H. Lee, D. Wang, Z. Ren, J.-P. Fleurial and P. Gonga, *Adv. Mater.* 19 (2007) p.1043.
- [17] Q. Zhang, J. He, S.N. Zhang, X.B. Zhao and T.M. Tritt, *J. Appl. Phys.* 93 (2008) p.102109.
- [18] W. Kim, J. Zide, A. Gossard, D. Klenov, S. Stemmer, A. Shakouri and A. Majumdar, *Phys. Rev. Lett.* 96 (2006) p.045901.
- [19] S. Bhattacharya, R.P. Hermann, V. Keppens, T.M. Tritt and G.J. Snyder, *Phys. Rev. B* 74 (2006) p.134108.
- [20] B.L. Pedersen, H. Birkedal, B.B. Iversen, M. Nygren and P.T. Fredriksen, *Appl. Phys. Lett.* 89 (2006) p.242108.
- [21] J. Choi, S.H. Tung, N.S. Wang and V. Reipa, *Nanotechnology* 19 (2008) p.085715.